

NASA/TP—2018-219517



# Microscale Fracture Testing of HfO<sub>2</sub>-Si Environmental Barrier Coatings

*Andrew L. Robertson*  
*University of Houston, Houston, Texas*

*Francisco Solá, Dongming Zhu, and Jon Salem*  
*Glenn Research Center, Cleveland, Ohio*

*Ken W. White*  
*University of Houston, Houston, Texas*

## NASA STI Program . . . in Profile

Since its founding, NASA has been dedicated to the advancement of aeronautics and space science. The NASA Scientific and Technical Information (STI) Program plays a key part in helping NASA maintain this important role.

The NASA STI Program operates under the auspices of the Agency Chief Information Officer. It collects, organizes, provides for archiving, and disseminates NASA's STI. The NASA STI Program provides access to the NASA Technical Report Server—Registered (NTRS Reg) and NASA Technical Report Server—Public (NTRS) thus providing one of the largest collections of aeronautical and space science STI in the world. Results are published in both non-NASA channels and by NASA in the NASA STI Report Series, which includes the following report types:

- TECHNICAL PUBLICATION. Reports of completed research or a major significant phase of research that present the results of NASA programs and include extensive data or theoretical analysis. Includes compilations of significant scientific and technical data and information deemed to be of continuing reference value. NASA counter-part of peer-reviewed formal professional papers, but has less stringent limitations on manuscript length and extent of graphic presentations.
- TECHNICAL MEMORANDUM. Scientific and technical findings that are preliminary or of specialized interest, e.g., “quick-release” reports, working papers, and bibliographies that contain minimal annotation. Does not contain extensive analysis.
- CONTRACTOR REPORT. Scientific and technical findings by NASA-sponsored contractors and grantees.
- CONFERENCE PUBLICATION. Collected papers from scientific and technical conferences, symposia, seminars, or other meetings sponsored or co-sponsored by NASA.
- SPECIAL PUBLICATION. Scientific, technical, or historical information from NASA programs, projects, and missions, often concerned with subjects having substantial public interest.
- TECHNICAL TRANSLATION. English-language translations of foreign scientific and technical material pertinent to NASA's mission.

For more information about the NASA STI program, see the following:

- Access the NASA STI program home page at <http://www.sti.nasa.gov>
- E-mail your question to [help@sti.nasa.gov](mailto:help@sti.nasa.gov)
- Fax your question to the NASA STI Information Desk at 757-864-6500
- Telephone the NASA STI Information Desk at 757-864-9658
- Write to:  
NASA STI Program  
Mail Stop 148  
NASA Langley Research Center  
Hampton, VA 23681-2199



# Microscale Fracture Testing of HfO<sub>2</sub>-Si Environmental Barrier Coatings

*Andrew L. Robertson*  
*University of Houston, Houston, Texas*

*Francisco Solá, Dongming Zhu, and Jon Salem*  
*Glenn Research Center, Cleveland, Ohio*

*Ken W. White*  
*University of Houston, Houston, Texas*

National Aeronautics and  
Space Administration

Glenn Research Center  
Cleveland, Ohio 44135

## Acknowledgments

This work is sponsored by Aeronautics Research Mission Directorate (ARMD) Transformational Tools & Technologies (TTT) project. A.L. Robertson was supported by the NASA Space Technology Research Fellowship, Grant NNX15AQ13H. The authors would like to acknowledge Dr. R. Rogers for the XRD work.

This work was sponsored by the  
Transformative Aeronautics Concepts Program.

Trade names and trademarks are used in this report for identification only. Their usage does not constitute an official endorsement, either expressed or implied, by the National Aeronautics and Space Administration.

*Level of Review:* This material has been technically reviewed by expert reviewer(s).

Available from

NASA STI Program  
Mail Stop 148  
NASA Langley Research Center  
Hampton, VA 23681-2199

National Technical Information Service  
5285 Port Royal Road  
Springfield, VA 22161  
703-605-6000

This report is available in electronic form at <http://www.sti.nasa.gov/> and <http://ntrs.nasa.gov/>

# Contents

Summary.....	1
1.0 Introduction .....	1
2.0 Experimental and Numerical Methods .....	2
2.1 Microcantilever Experimental Method .....	2
2.2 Microcantilever Numerical Method .....	3
2.3 Single-Edge V-Notched Beam Experimental Method .....	4
3.0 Results .....	4
3.1 Microstructure Characterization.....	4
3.2 Microcantilever Experimental Results .....	4
3.3 Microcantilever Numerical Results.....	8
3.4 Single-Edge V-Notched Beam .....	10
4.0 Discussion.....	11
4.1 Crack Geometry Effect on Calculation of Fracture Toughness.....	11
4.2 Microstructure Effect on Fracture Toughness.....	11
4.3 Method Limitations.....	12
4.4 Comparisons With Bulk Specimens.....	13
5.0 Conclusions .....	13
Appendix.—Load-Displacement Fracture Demonstration .....	15
References .....	16



# Microscale Fracture Testing of HfO<sub>2</sub>-Si Environmental Barrier Coatings

Andrew L. Robertson  
University of Houston  
Houston, Texas 77204

Francisco Solá, Dongming Zhu, and Jon Salem  
National Aeronautics and Space Administration  
Glenn Research Center  
Cleveland, Ohio 44135

Ken W. White  
University of Houston  
Houston, Texas 77204

## Summary

Environmental barrier coatings (EBCs) play a vital role in protecting advanced turbine components constructed from ceramic matrix composites. EBC performance is evaluated based on many factors such as mechanical and thermal properties and chemical stability. This study focuses on the mechanical properties of individual phases within a HfO<sub>2</sub>-Si EBC through the combined use of chevron-notched microcantilevers and finite element modeling. The Si- and HfO<sub>2</sub>-rich phases were found to have fracture toughness  $K_{IC}$  values of  $1.36 \pm 0.07$  MPa·m<sup>1/2</sup> and  $1.99 \pm 0.36$  MPa·m<sup>1/2</sup>, respectively. Despite irregular notch geometry, calculated  $K_{IC}$  values agreed reasonably with literature values of monolithic samples for the respective phases. The relatively large scatter in the HfO<sub>2</sub>-rich samples is attributed to heterogeneity in fracture feature size and distribution of the HfO<sub>2</sub> and HfSiO<sub>4</sub> phases. Comparisons with bulk single-edge V-notched beams suggest bulk behavior is dictated by the fracture behavior of the Si-rich phase with no contribution from the HfO<sub>2</sub>-rich phase.

## 1.0 Introduction

Ceramic matrix composites (CMCs) are enabling cleaner, more efficient aircraft engines. These materials are primarily targeted as components for the hot section of turbine engines, with capabilities set by inlet temperatures. CMCs with 1,315 °C capability began flying in commercial aircraft engines in the year 2016. NASA is currently developing CMCs and environmental barrier coatings (EBCs) with greater temperature capabilities (up to 1,482 °C), which would both reduce fuel burn by ~6 percent and decrease emissions. However, CMCs suffer significant recession (material loss) with exposure to turbine conditions. To mitigate recession, CMCs are protected with EBCs (Ref. 1). The performance of the advanced EBCs is multifaceted with

consideration given to thermomechanical stresses, creep resistance, temperature-dependent mechanical properties, environmental and chemical stability, and thermal properties (Refs. 1 to 3). HfO<sub>2</sub>-Si is one EBC bond coat system that has been developed with higher temperature capability and improved strength and stability for 2,700 °F EBC applications (Ref. 3). EBCs, often composites themselves, exhibit complex mechanical behavior involving multiple failure mechanisms similar to traditional ceramic composites (Ref. 4). Traditional macroscale tests can provide effective mechanical properties, but they offer limited information on the contributions of individual phases within the EBC. Alternatively, microscale tests yield local microstructure properties that enable better microstructure development for optimized effective properties. Several studies have employed such micromechanical tests to measure the mechanical properties of coatings (Refs. 5 to 7).

Microcantilever beams machined by a focused ion beam (FIB) are among the most popular test specimens for performing microscale mechanical experiments and discerning otherwise unobtainable local microstructure properties. For example, microcantilevers were utilized by Gong and Wilkinson to study the critical resolved shear stress of an  $\alpha$ -Ti alloy (Ref. 8). Also, Tatami et al. studied the grain boundary toughness of Si<sub>3</sub>N<sub>4</sub> ceramics with different rare earth additives and their effect on crack-growth-resistance (*R*-curve) behavior (Ref. 9). When employing FIB-machined specimens it is important to consider the effect that ion milling has on the specimen microstructure. FIB milling has been shown to induce microstructural changes such as amorphization and nucleation of dislocations and point defects as well as directly change mechanical properties through the development of residual compressive stresses from ion implantation (Refs. 10 and 11). To minimize these milling effects, multiple approaches have been developed. Sebastiani et al. developed a novel test

whereby a sharp Berkovich indenter is used to split a FIB-milled micropillar (Ref. 5). The authors hypothesized that the majority of the cracked regions reside in the volume with sufficient distance from the milled surfaces. Alternatively, Mueller et al. tested chevron-notched microcantilevers where a sharp crack is nucleated at the apex of the chevron, and stable crack growth occurs prior to unstable fracture (Ref. 12). The extent of this stable crack growth ensures that all but the edges of the crack front are free from milling damage.

This study utilizes FIB-milled chevron-notched microcantilever beams, as described in the literature (Ref. 13), coupled with finite element method (FEM) modeling to extract the fracture toughness of individual phases in a  $\text{HfO}_2\text{-Si}$  composite EBC. Single-edge V-notched beam (SEVNB) testing of comparable bulk specimens was also performed for comparison with the microscale tests.

## 2.0 Experimental and Numerical Methods

$\text{HfO}_2\text{-Si}$  EBC specimens were prepared through a hot-press process using the NASA composition and particle size specification plasma spray coating powders (silicon-clad  $\text{HfO}_2$  powders, designation AE10218, Oerlikon Metco, New York). The bulk  $\text{HfO}_2\text{-Si}$  specimens were tested because of the advantages to obtain composite coating material overall mechanical properties, and then correlated and compared to the measured micromechanical properties obtained by the FIB microcantilever beam method. Raw composite coating powders of  $\text{HfO}_2\text{-Si}$  (Oerlikon Metco) were inserted into a graphite die with the dimension of 50 by 76 by 10 mm, then heated to 1,350 °C in vacuum and subjected to 103.5 MPa (15 ksi) of pressure for 2 h processing. The hot-processed  $\text{HfO}_2\text{-Si}$  composite plates were then machined to produce 3- by 4- by 50-mm bar specimens for microstructure characterization and mechanical property testing. Secondary electron (SE) images taken at 5 keV, were collected by a dual-beam microscope (Auriga, Carl Zeiss NTS GmbH). Backscattered-electron (BSE) microscopy images were collected by a Hitachi S4700 instrument operated at 25 keV. X-ray diffraction (XRD) (D8 Advance Diffractometer, Bruker) with  $\text{Cu K}\alpha$  radiation was done for microstructure characterization. Transmission electron microscopy (TEM) was performed with a FEI Image Corrected Titan3™ G2 60-300 S/TEM in scanning mode and operating at 300 keV. TEM sample preparation was done with standard dual-beam FIB methods, followed by Fischione 1040 argon ion milling.

### 2.1 Microcantilever Experimental Method

A  $\text{Ga}^+$  FIB (Auriga, Carl Zeiss) was used to machine chevron-notched triangular microcantilever beams rich in  $\text{HfO}_2$

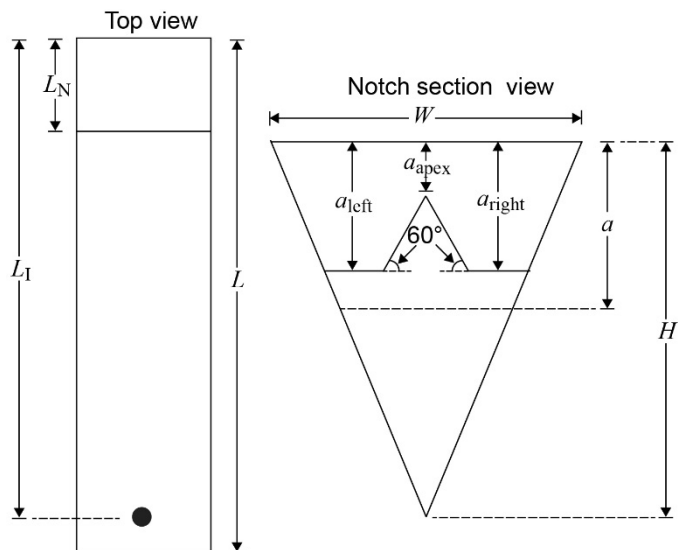


Figure 1.—Fabricated microcantilevers where  $L$  is length,  $L_N$  is length to notch,  $L_I$  is length to indent,  $W$  is width,  $H$  is height,  $a_{\text{apex}}$  is length to chevron apex,  $a_{\text{left}}$  is length to left shoulder,  $a_{\text{right}}$  is length of right shoulder, and  $a$  is length to crack front.

or Si phases, using methods similar to those described in the literature (Ref. 13). Rough cuts, fine cuts, and notching were performed at 2 nA, 600 pA, and 10 pA beam currents, respectively. A chevron notch was desired for the purposes of allowing a “pop-in” event to occur followed by stable crack growth prior to unstable fracture. Figure 1 shows a schematic of a typical resultant microcantilever and a section view of the notch geometry. Although a full chevron was the desired geometry, the samples typically possessed an undercut chevron with shoulders of heights  $a_{\text{left}}$  and  $a_{\text{right}}$ , with  $a_{\text{left}}$  not necessarily equal to  $a_{\text{right}}$ . For samples with this undercut chevron, unstable fracture is expected at a crack length of either  $a_{\text{left}}$  or  $a_{\text{right}}$ , whichever is longer. At this point, the crack front will not only extend abruptly, but also represent the point of the widest crack front beyond which the crack front width will decrease. In practice, crack stability is complex and involves consideration of specimen geometry, tester compliance, and material toughness; this will be discussed more in Sections 3.2 and 4.1. An in situ PicoIndenter 85 (Hysitron, Inc.) was used to position a 30-nm-radius cube-corner diamond indenter tip (Refs. 14 and 15) over the free end of a microcantilever and deflect the microcantilever under displacement control at a rate of 15 nm/s while recording load-displacement data and SE video. To correct for indenter penetration into each microcantilever, reference indents were performed in each phase, and the average displacement for a given load was subtracted from the load-displacement data collected during the testing. Posttest fracture surfaces were inspected for notch dimensions and phase fracture mechanisms.



## 2.2 Microcantilever Numerical Method

ABAQUS 6.14 (Dassault Systèmes Simulia Corp.) was used to model each tested microcantilever. As each beam varied slightly in dimensions, measurements of the dimensions of each beam pretest and posttest were used for their respective models. The elastic moduli of each beam was inputted according to its respective phase: 169 GPa for the HfO<sub>2</sub>-rich phase and 171 GPa for the Si-rich phase as measured by nanoindentation. Encastre boundary conditions (i.e., fixed in all degrees of freedom) were placed on the fixed end of the beam, whereas the free end along the top edge was prescribed a uniform displacement downward.

For each microcantilever, two separate simulations were performed. The notched, but uncracked, specimen geometry was loaded to the experimental elastic limit to ensure that the calculated compliance fit the experimental compliance. This simulation served as a check that the microcantilever model dimensions were indeed correct. This model was meshed using second-order hexahedral elements without mesh refinement near the chevron notch, as the global load-displacement response should depend minimally on the accuracy within this small region (Ref. 16). A model was then generated with a crack length,  $a$ , corresponding to the position of widest crack front according to the fractured surface. For most specimens, this crack length corresponded to either  $a_{\text{left}}$  or  $a_{\text{right}}$  depending on which was the longer of the two. This model was prescribed the displacement recorded at maximum load after a pop-in event had occurred. For one specimen that had a full chevron notch, a best judgement was made based on the fracture surface as to the position of the crack front at the desired load.

The cracked model was meshed with second-order tetrahedron elements outside the crack tip region (Figure 2(a)) and in the crack tip region, a cylinder of concentric rings of second-order hexahedral elements with an inner ring of second-order degenerate hexahedral elements at the crack front (Figure 2(b)). The cylindrical mesh of the crack tip was limited to a fraction,

typically between 0.7 and 0.9, of the total width of the crack front because of limitations in the native meshing algorithm for producing a symmetric structured mesh of concentric rings with out-of-plane boundaries.

To generate the  $r^{-1/2}$  singularity found in linear elastic fracture mechanics, the midpoint nodes were moved to  $1/4$  position between crack tip nodes and the adjacent vertex nodes of second-order degenerate hexahedral elements with the crack tip side collapsed to a single edge (Ref. 17). The calculation of the mode I stress intensity factor,  $K_I$ , was performed using contour integrals in the focused mesh region around the crack tip for an assumed crack propagation direction in the direction of loading. As in Reference 18, the  $J$ -integral is defined as

$$J = \oint_{\mathbf{G}} W dy - \int_{\Gamma} \frac{\mathbf{T} \cdot \mathbf{u}}{dx} ds \quad (1)$$

where  $\mathbf{G}$  is the closed loop around the crack,  $W$  is the strain energy density function,  $\mathbf{T}$  is the outward normal traction vector, and  $\mathbf{u}$  is the displacement vector. For linear elastic materials  $J$  is path independent and  $J = G$ , where  $G$  is the strain energy release rate, and is related to the mode I, II, and III stress intensity factors  $K_I$ ,  $K_{II}$ , and  $K_{III}$ , respectively, by

$$J = G = \frac{1 - \nu^2}{E} (K_I^2 + K_{II}^2) + \frac{1 + \nu^2}{E} (K_{III}^2) \quad (2)$$

where  $\nu$  is the Poisson ratio and  $E$  is the elastic modulus (Ref. 18). The fracture toughness  $K_C$  for each sample is determined by the mean  $K_I$  of the final contour integral at each point along the crack front. In general, mixed-mode problems require the use of interaction integrals (Ref. 19) for determination of individual contributions of  $K_I$ ,  $K_{II}$ , and  $K_{III}$ , but under pure bending  $K_{II}$  and  $K_{III}$  contributions are negligible and are not considered here.

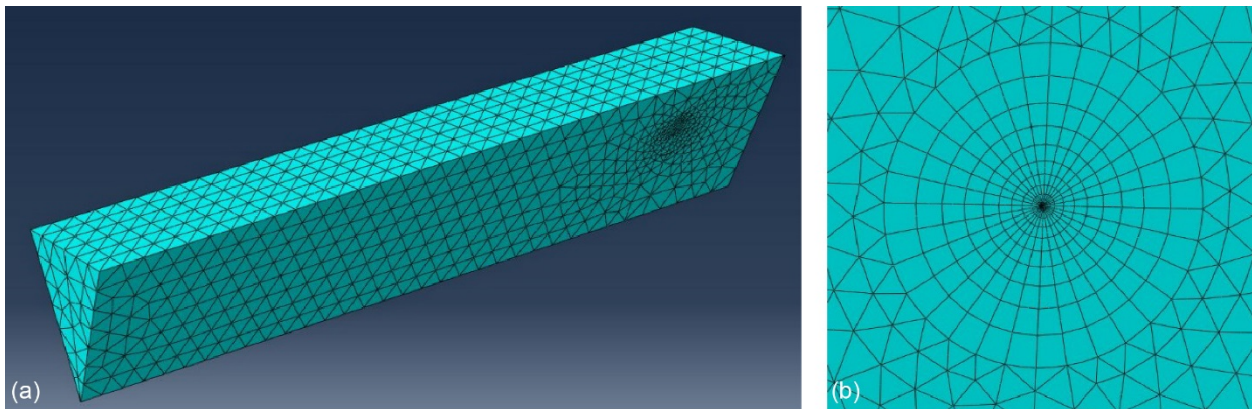


Figure 2.—Microcantilever model mesh composed of second-order tetrahedral elements. (a) Full microcantilever model. (b) Structured, focused mesh at crack tip composed of concentric rings of second-order hexahedral elements with ring of second-order degenerate hexahedral elements at crack tip.

### 2.3 Single-Edge V-Notched Beam Experimental Method

Three bulk SEVNB specimens of nominal dimensions 3 by 5 by 25 mm with a sawn V-notch of nominal crack length:height ratio  $a/w$  of 0.2 were tested under four-point bending with 10 and 20 mm inner and outer spans, respectively. Tests were performed on a screw-driven load frame (Instron 8562) in displacement control at a displacement rate of 0.25 mm/min. Fracture toughness was evaluated according to ISO 23146 (Ref. 20).

## 3.0 Results

Results from the microstructure analysis of the Hf-SiO<sub>2</sub> systems by SEM and high-resolution TEM (HRTEM) analyses are presented as are results from the mechanical tests and numerical analyses of the microcantilever and SEVNB specimens.

### 3.1 Microstructure Characterization

The resultant microstructure (Figure 3) included two primary phases composed of Si and HfO<sub>2</sub>-HfSiO<sub>4</sub>.

The hafnia phase was composed primarily of hafnia, HfO<sub>2</sub> (or a small amount of Si-soluble HfO<sub>2</sub>), and a small amount of hafnium silicate, HfSiO<sub>4</sub>, also known as hafnon. The HfO<sub>2</sub> phase also contained a relatively small amount of porosity. As the hafnia and hafnon phases could not be easily separated in terms of mechanical testing, the phase containing both hafnia and hafnon is simply referred to as “HfO<sub>2</sub>-rich” for the remainder of the report. The Si-rich phase also contained a small amount of HfO<sub>2</sub>-HfSiO<sub>4</sub> inclusions.

XRD analysis (Figure 4) confirmed the presence of cubic phase Si, monoclinic HfO<sub>2</sub>, and tetragonal HfSiO<sub>4</sub>. For Si, the lattice parameters were calculated to be  $a = b = c = 5.4293 \text{ \AA}$ ; for HfO<sub>2</sub>  $a = 5.12153 \text{ \AA}$ ,  $b = 5.16580 \text{ \AA}$ , and  $c = 5.31384 \text{ \AA}$ ; and for HfSiO<sub>4</sub>  $a = b = 6.57231 \text{ \AA}$  and  $c = 5.97034 \text{ \AA}$ . Quantitative phase analysis calculated using whole pattern fitting (WPF) and Rietveld refinement method, resulted in estimations of  $70.3 \pm 0.4 \text{ wt\%}$  for Si,  $24.9 \pm 0.2 \text{ wt\%}$  for HfO<sub>2</sub>, and  $4.8 \pm 0.1 \text{ wt\%}$  for HfSiO<sub>4</sub> phases.

Figure 5(a) is a HRTEM image of the Si matrix. The splitting of the Si dumbbell atoms are clearly seen, with a  $\langle 112 \rangle$  crystallographic orientation. Figure 5(b) is a HRTEM image of the HfO<sub>2</sub>-HfSiO<sub>4</sub> composite structure, note that their interphase is not coherent. Figure 5(c) is a closeup of the region enclosed by the white square in Figure 5(b), which reveals (101) Hf(SiO<sub>4</sub>)

fringes with an interplanar distance of  $4.52 \text{ \AA}$ , which further confirms the tetragonal structure of HfSiO<sub>4</sub>. Figure 5(d) is a closeup of the region enclosed by the black square in Figure 5(b). Similar analysis reveals the (111) HfO<sub>2</sub> monoclinic interplanar spacing of  $2.83 \text{ \AA}$ .

### 3.2 Microcantilever Experimental Results

Typical HfO<sub>2</sub>- and Si-rich phase microcantilever beams of nominal dimensions  $17 \text{ \mu m}$  length by  $3 \text{ \mu m}$  width by  $4 \text{ \mu m}$  height are shown in Figure 6 with Table I tabulating the dimensions of the seven successfully tested samples.

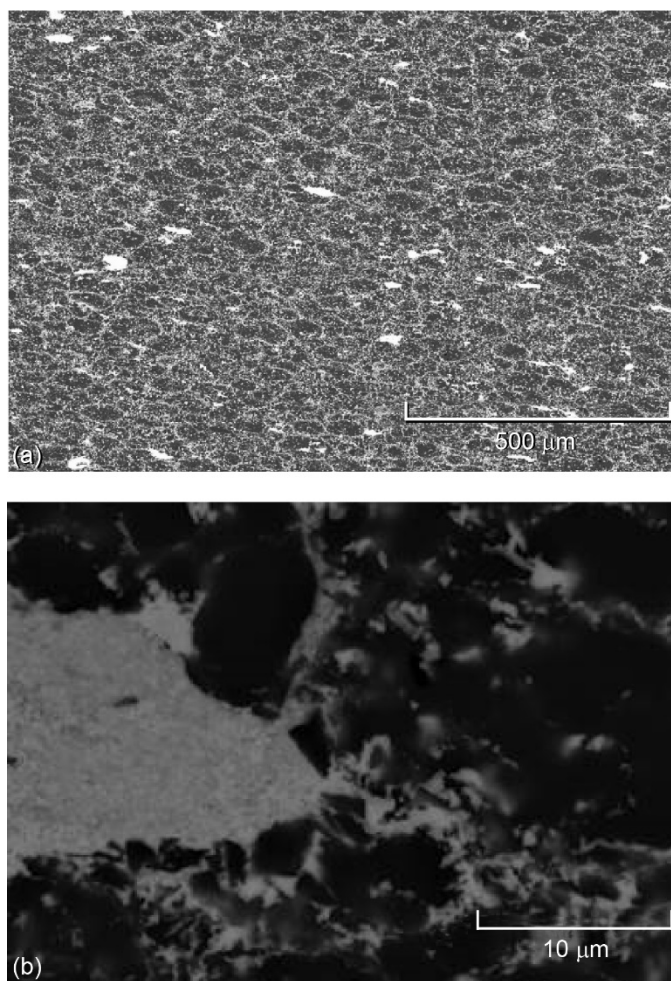


Figure 3.—Scanning Electron Microscope (SEM) images of hot-pressed HfO<sub>2</sub>-Si microstructure. Light phase is composed of HfO<sub>2</sub> and HfSiO<sub>4</sub>, and dark phase is Si rich with HfO<sub>2</sub> and HfSiO<sub>4</sub> inclusions. (a) Low-magnification secondary electron (SE) micrograph. (b) Backscattered SE micrograph.

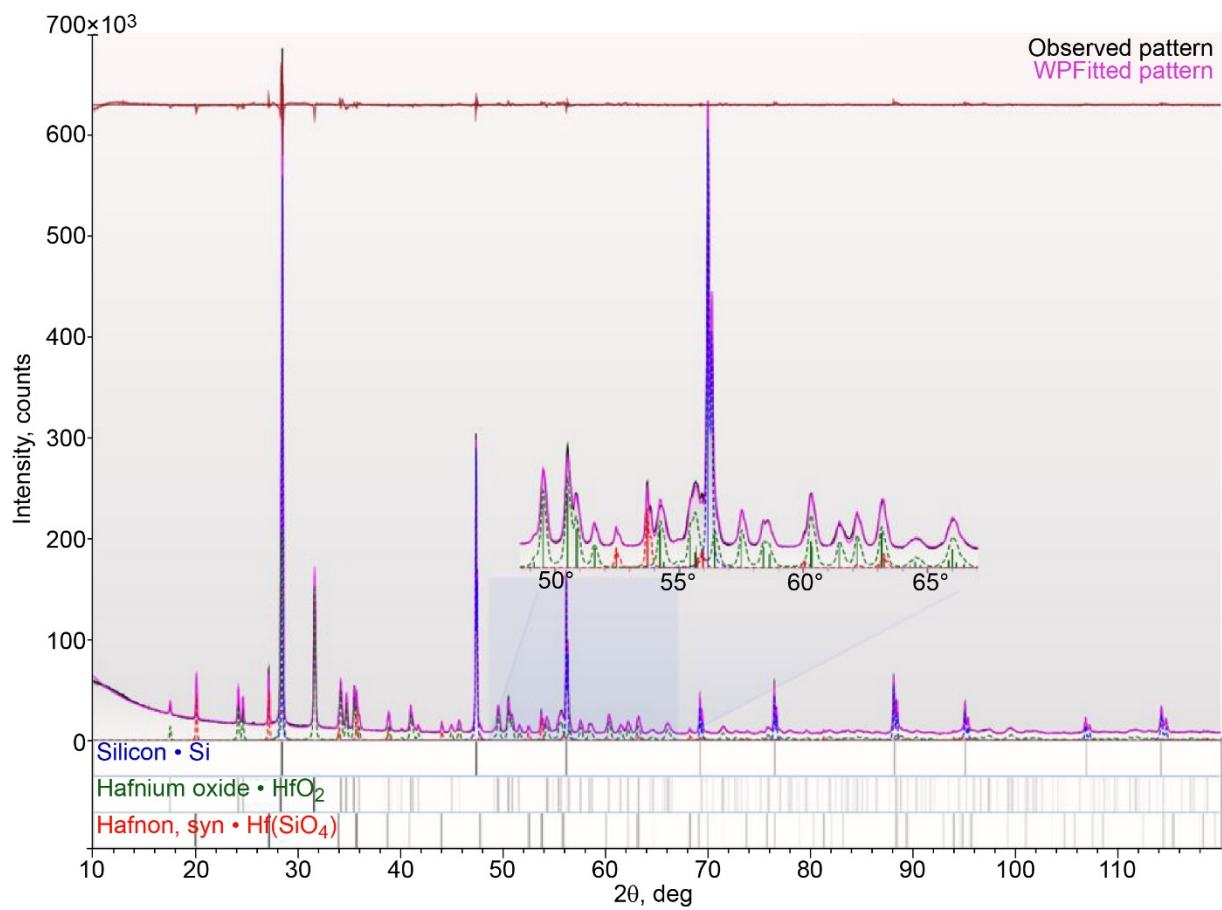


Figure 4.—X-ray diffraction intensity versus  $2\theta$  for hot-pressed HfO<sub>2</sub>-Si, showing presence of cubic Si, monoclinic HfO<sub>2</sub>, and tetragonal HfSiO<sub>4</sub>.

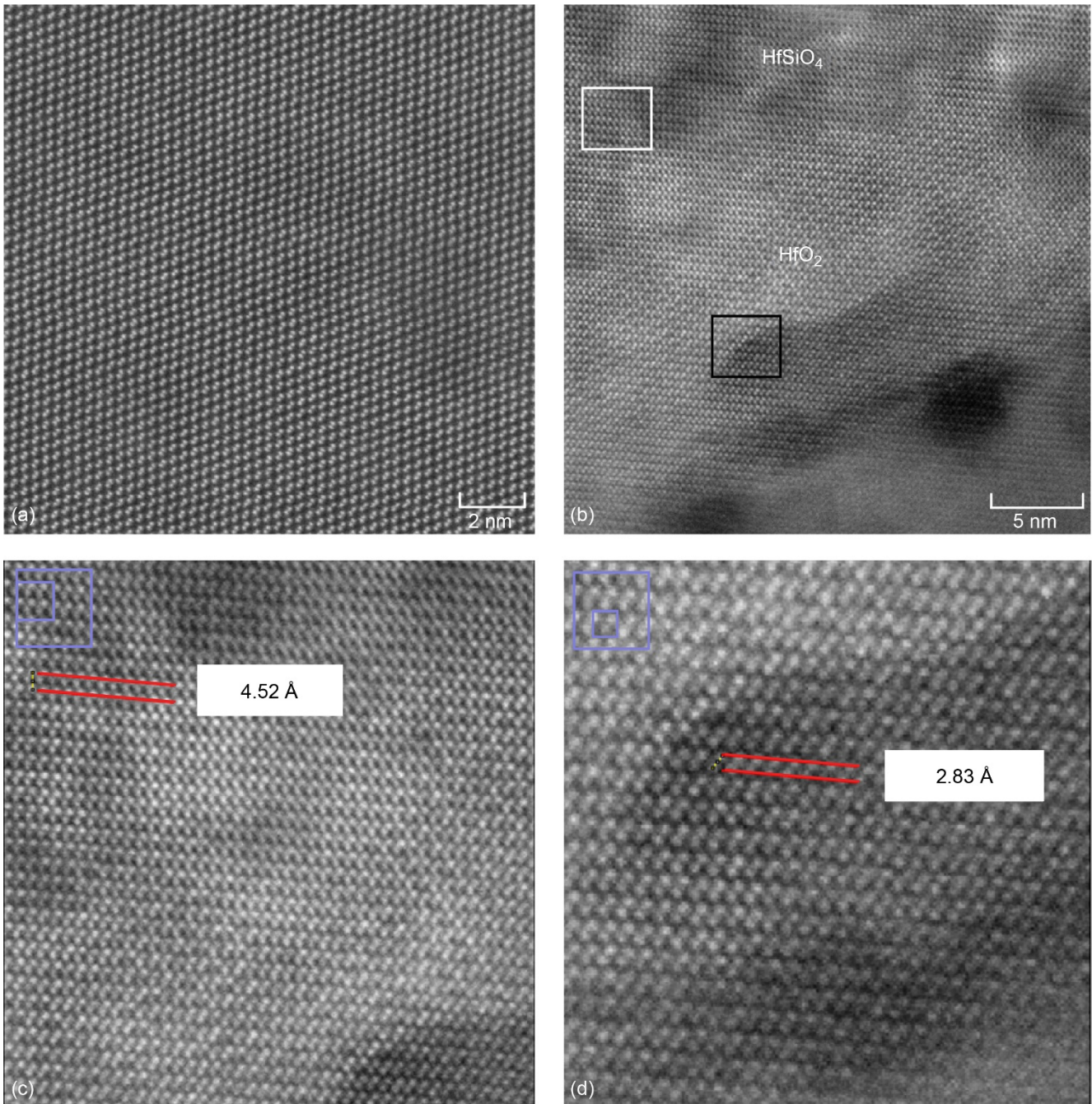


Figure 5.—High-resolution transmission electron micrographs (HRTEMs) of hot-pressed  $\text{HfO}_2$ -Si. (a) Si matrix. (b)  $\text{HfO}_2$ - $\text{HfSiO}_4$  inclusions. (c) Closeup of  $\text{HfSiO}_4$  structure in (b) showing 4.52-Å spacing of (101) plane. (d) Closeup of  $\text{HfO}_2$  structure in (b) showing 2.83-Å spacing of (111) plane.

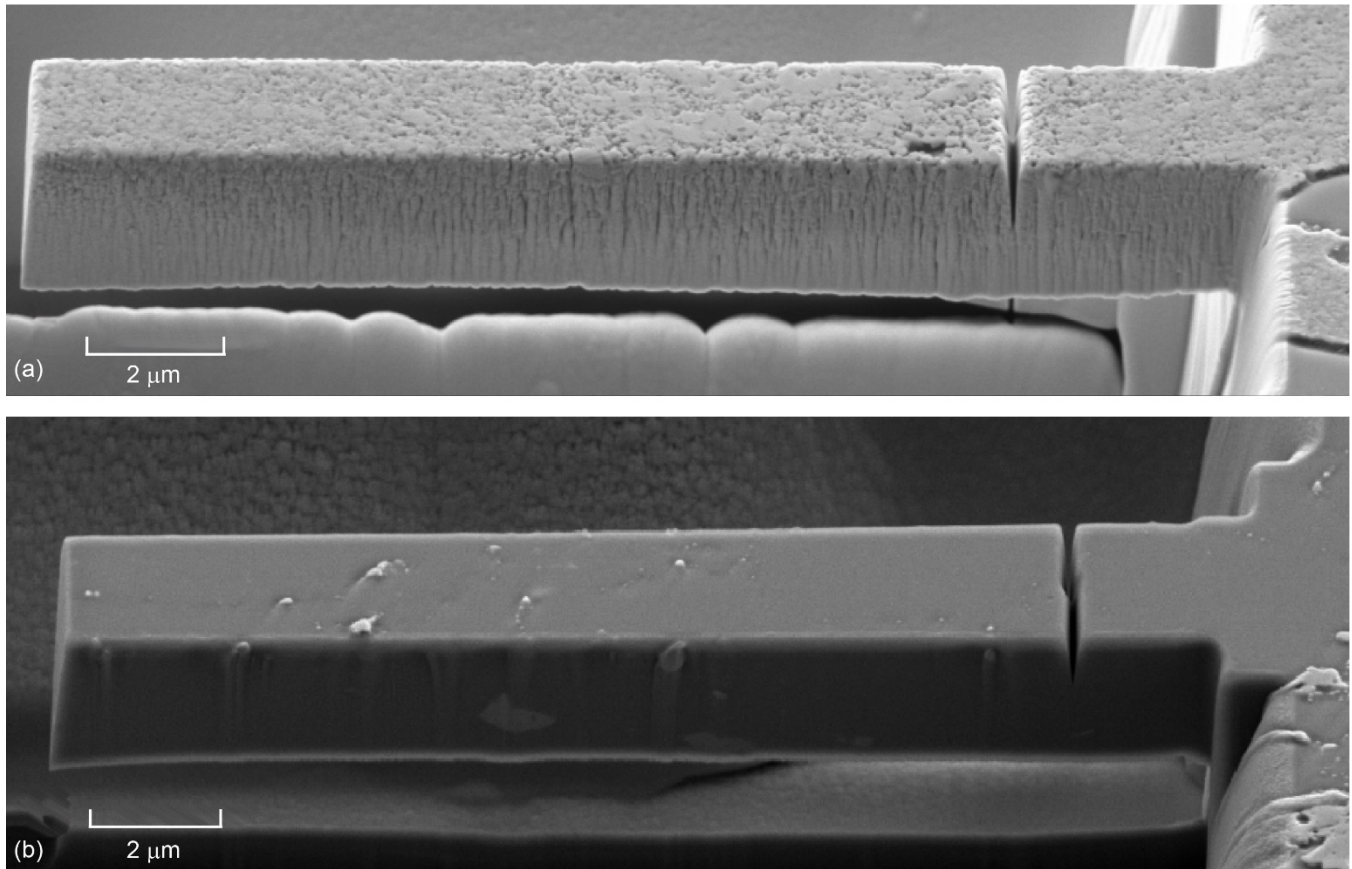


Figure 6.—Typical machined HfO<sub>2</sub>-Si microcantilever beams. Nominal dimensions of 17 μm length by 3 μm width by 4 μm height. (a) HfO<sub>2</sub>-rich phase. (b) Si-rich phase.

TABLE I.—HfO<sub>2</sub>-HfSiO<sub>4</sub> MICROCANTILEVER SPECIMEN DIMENSIONS<sup>a</sup>

Specimen	Height, <i>H</i> , mm	Width, <i>W</i> , mm	Length, <i>L</i> , mm	Length to notch, <i>L<sub>N</sub></i> , mm	Length to indent, <i>L<sub>I</sub></i> , mm	Chevron precrack dimensions		
						Length to apex, <i>a<sub>apex</sub></i> , mm	Length to left shoulder, <i>a<sub>left</sub></i> , mm	Length to right shoulder, <i>a<sub>right</sub></i> , mm
Si-rich 1	3.24	2.92	18.11	2.39	17.47	0.49	1.21	1.21
Si-rich 2	4.63	3.56	15.73	3.38	15.12	0.61	1.57	1.57
Si-rich 3	4.31	3.41	17.22	3.04	16.32	0.62	1.49	1.85
Si-rich 4	4.08	3.31	17.40	2.69	15.93	0.65	1.56	2.03
HfO <sub>2</sub> -rich 1	3.27	3.22	16.34	2.18	15.36	0.91	1.38	1.57
HfO <sub>2</sub> -rich 2	4.73	3.97	16.69	3.26	15.31	0.98	1.41	1.70
HfO <sub>2</sub> -rich 3	3.59	2.43	17.46	3.35	15.79	0.60	1.84	1.62

<sup>a</sup>Dimensions listed in Figure 1.

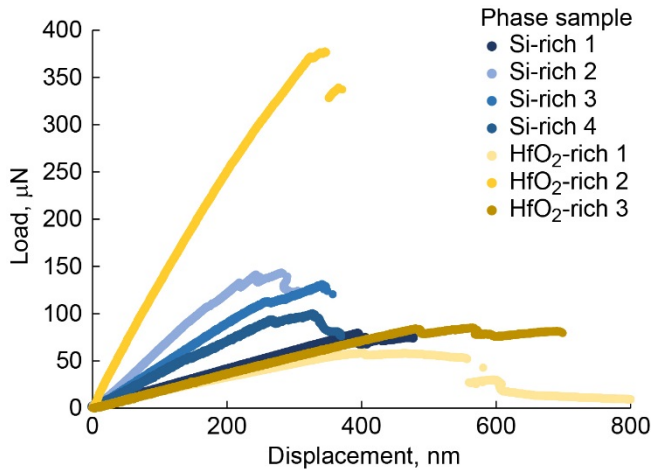


Figure 7.—Corrected load-displacement curves for tested HfO<sub>2</sub>-Si microcantilevers.

Video recordings alongside load-displacement data (see supplementary information) during each test confirmed that pop-in events corresponded to jumps in crack mouth opening displacement that indicate subcritical crack growth. Figure 7 plots the corrected load-displacement data (see Sec. 2.1 for correction procedure) for the seven successfully tested microcantilevers, where the different colors represent individual microcantilevers. Note the common features of pop-ins among all samples and stable crack growth beyond a maximum load in a few samples. Among all of the samples, a couple recurring features were found: First, pop-in events of varying magnitude were found in all samples with some samples having two pop-in events. Second, some samples exhibited decreasing load with increasing displacement, indicating crack stability under displacement control. Although the main features of the load-displacement curves were similar, the variations in number of pop-in events and presence or absence of crack stability beyond a maximum load could most likely be attributed to the variations in initial crack geometry and/or phase properties and subsequent propagation.

Figure 8 compares the fracture surfaces of HfO<sub>2</sub>-rich and Si-rich microcantilevers; the red lines indicate the crack front position that was modeled. In most cases, the chevron was not

fully cut, which resulted in an irregular geometry. This irregular geometry consisted of an undercut chevron with shoulders that may or not be of the same height. Pop-in events on the load-displacement plot (Figure 7) represent nucleation of a sharp crack at the apex of the chevron, and further crack extension will be accompanied by an increase in load. Once the crack front reaches a shoulder where the crack front abruptly increases in width, an increase in load is required to continue crack extension. The crack front is widest at this point and will correspondingly sustain the highest load. The most prominent difference between the HfO<sub>2</sub>-rich and Si-rich phases is the type of fracture they undergo: intergranular fracture in the HfO<sub>2</sub>-rich phase and cleavage in the Si-rich phase. In the HfO<sub>2</sub>-rich phase exists small grains, on the order of 100 nm in diameter, which contribute greatly to promoting intergranular fracture, whereas the micron-sized grains in the Si-rich phase promote transgranular cleavage. The low phase contrast of the fracture surfaces prevented determination of the individual roles played by the HfO<sub>2</sub> and HfSiO<sub>4</sub> phases during fracture.

### 3.3 Microcantilever Numerical Results

Table II lists the numerical inputs of crack length  $a$  determined from the specimen fracture surfaces; displacement  $\Delta$  recorded at the maximum load  $P_{\max}$  after a pop-in; and the apparent experimental compliance  $C_{\text{exp}}$  at this point for each specimen and the corresponding  $K_C$ ,  $P_{\max, \text{FEM}}$ , and apparent  $C_{\text{FEM}}$  for the respective FE models with the imposed displacement  $\Delta$  as well as the  $C_{\text{FEM}}$  error. The  $C_{\text{FEM}}$  error was defined as  $(C_{\text{FEM}} - C_{\text{exp}})/C_{\text{exp}} \cdot 100$ . In general, the crack length was taken to be the longer of  $a_{\text{left}}$  or  $a_{\text{right}}$  as listed in Table I, except in two specimens, Si-rich cantilever 4 and HfO<sub>2</sub>-rich cantilever 3. For these specimens, it was found that the  $C_{\text{FEM}}$  error at crack lengths of  $a_{\text{left}}$  or  $a_{\text{right}}$  were much too large. As such, the most likely positions of the crack fronts were then chosen based on the features of the fracture surface as shown in Figure 8. Although this approach seemed to work for HfO<sub>2</sub>-rich cantilever 3, the  $C_{\text{FEM}}$  error for Si-rich cantilever 4 is still greater than 10 percent and its  $K_C$  may be erroneous. This process is not strictly rigorous and may result in additional error to the calculation of  $K_C$ .

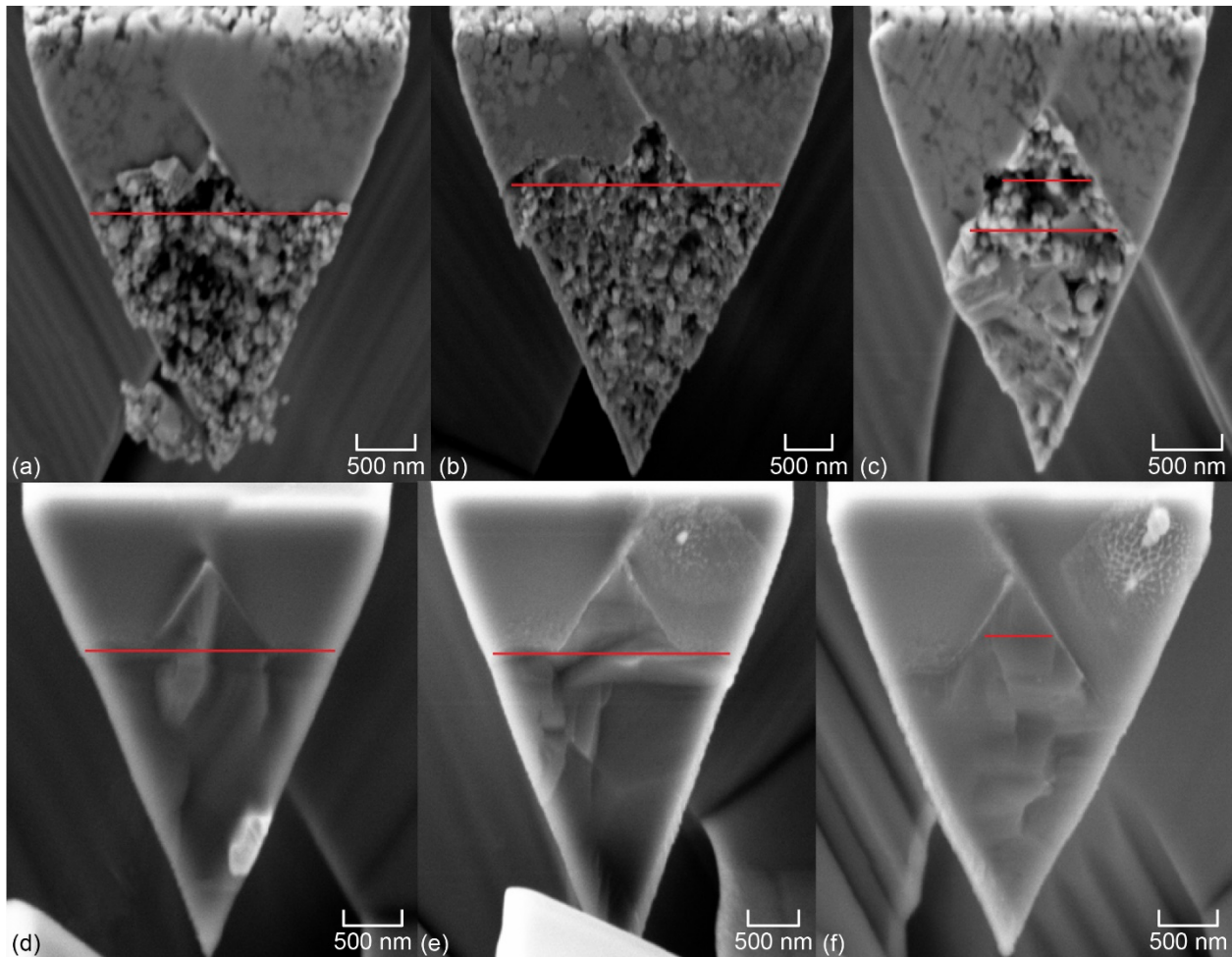


Figure 8.—HfO<sub>2</sub>-Si microcantilever fracture surfaces (Tables I and II). Red lines indicate position of crack front used in finite element models. (a) HfO<sub>2</sub>-rich cantilever 1. (b) HfO<sub>2</sub>-rich cantilever 2. (c) HfO<sub>2</sub>-rich cantilever 3. (d) Si-rich cantilever 1. (e) Si-rich cantilever 2. (f) Si-rich cantilever 4.

TABLE II.—EXPERIMENTAL AND NUMERICAL RESULTS FOR HfO<sub>2</sub>-Si MICROCANTILEVER BEAM SPECIMENS

Specimen	Experimental				Numerical <sup>a</sup>		
	Crack length, $a$ , $\mu\text{m}$	Maximum load, $P_{\text{max}}$ , $\mu\text{N}$	Displacement, $\Delta$ , nm	Compliance, $C_{\text{exp}}$ , nm/ $\mu\text{N}$	Maximum load, $P_{\text{max,FEM}}$ , $\mu\text{N}$	Compliance (percent error), $C_{\text{FEM}}$ , nm/ $\mu\text{N}$	Fracture toughness, $K_{\text{C}}$ , $\text{MPa}\cdot\text{m}^{1/2}$
Si-rich 1	1.21	74.5	476.4	6.4	70.7	6.7 (5.3)	1.43
Si-rich 2	1.57	143.0	281.5	2.0	144.7	1.9 (-1.2)	1.36
Si-rich 3	1.85	131.1	341.4	2.6	128.3	2.7 (2.2)	1.27
Si-rich 4	1.20	100.2	327.3	3.3	89.8	3.6 (11.6)	1.36
HfO <sub>2</sub> -rich 1	1.57	57.5	470.0	8.2	56.7	8.3 (1.3)	1.55
HfO <sub>2</sub> -rich 2	1.70	339.1	366.0	1.1	326.5	1.1 (3.9)	1.87
HfO <sub>2</sub> -rich 3A	1.32	84.9	566.5	6.7	86.7	6.5 (-2.1)	2.18
HfO <sub>2</sub> -rich 3B	1.62	80.6	697.0	8.6	79.3	8.8 (1.6)	2.37

<sup>a</sup>From finite element method (FEM) analysis using ABAQUS (Dassault Systèmes Simulia Corp.).

Table III gives  $K_{IC}$ , taken as the average  $K_C$ , and average  $C_{FEM}$  error for the HfO<sub>2</sub>-rich and Si-rich phase models. The low average and much higher error in the  $C_{FEM}$  error is because the compliance of the model can be either higher or lower than its experimental counterpart. The HfO<sub>2</sub>-rich samples had a  $K_{IC}$  of  $1.99 \pm 0.57$  MPa·m<sup>1/2</sup> compared with the lower value of  $1.36 \pm 0.10$  MPa·m<sup>1/2</sup> found for the Si-rich samples where the bounds are the 95% confidence interval. The larger toughness in the HfO<sub>2</sub>-rich samples is likely due to the intergranular fracture mechanism and the increased scatter from microstructural heterogeneity at the scale of the test specimens. The Si-rich samples, on the contrary, had slightly lower toughness, but considerably less scatter.  $K_{IC}$  for both HfO<sub>2</sub>-rich and Si-rich phases match literature  $K_{IC}$  values for monolithic samples of 2 MPa·m<sup>1/2</sup> (Ref. 21) and 1.3 MPa·m<sup>1/2</sup> (Ref. 22) for the respective phases, although the  $K_{IC}$  for the Si-rich samples is at most 0.6 MPa·m<sup>1/2</sup> higher than the literature values and could be due to the incomplete chevron having a significant portion of the crack front directly exposed to ion milling and, consequently, compressive ion implantation stresses (Ref. 7). The reported values for HfO<sub>2</sub> involved monolithic HfO<sub>2</sub> that contained no HfSiO<sub>4</sub>.

A typical plot of calculated  $K_I$  values found across the crack front is shown in Figure 9. A straight front exhibited slight lowering of  $K_I$  with proximity to the sides of the microcantilever. This effect is likely due to the lowering of the constraint near the edges. The edges of the crack front approach a plane stress condition, whereas the center of the crack is under plane strain. Nevertheless, the effect is minimal and can be considered a small,  $\sim 0.01$  MPa·m<sup>1/2</sup>, uncertainty in the average  $K_C$  for the sample. The calculation of  $K_I$  was stable through seven contours, lending confidence in the numerical accuracy of the final result. This behavior was observed in all samples.

### 3.4 Single-Edge V-Notched Beam

A typical load versus back-face strain plot collected during SEVNB testing is shown in Figure 10. Linear elastic behavior is observed prior to a slight nonlinearity prior to fracture. This nonlinearity may be evidence of stable crack growth prior to unstable fracture; however, this behavior was not investigated.  $K_{IC}$  was calculated as the average of the three tested specimens and was  $1.1 \pm 0.1$  MPa·m<sup>1/2</sup>. A typical fracture surface is shown in Figure 11 where it is shown that the Si-rich phase fractured through cleavage and the HfO<sub>2</sub>-rich phase fractured intergranularly, the same mechanisms found in the microcantilever specimens. From the fracture surface, approximately 59 percent of the area consisted of the HfO<sub>2</sub>-rich phase, and the remaining 41 percent was made up of the Si-rich phase.

TABLE III.—AVERAGE CALCULATED  $K_{IC}$  AND LOAD PERCENT DIFFERENCE FOR SIMULATED HfO<sub>2</sub> AND Si PHASE MICROCANTILEVERS<sup>a</sup>

Phase	Mode I fracture toughness, $K_{IC}$ , MPa·m <sup>1/2</sup>	Average error in compliance $C_{FEM}$ , percent
HfO <sub>2</sub> -rich	$1.99 \pm 0.57$	$0.08 \pm 3.94$
Si-rich	$1.36 \pm 0.10$	$4.46 \pm 8.65$

<sup>a</sup>Finite element method (FEM) simulations performed with ABAQUS (Dassault Systèmes Simulia Corp.).

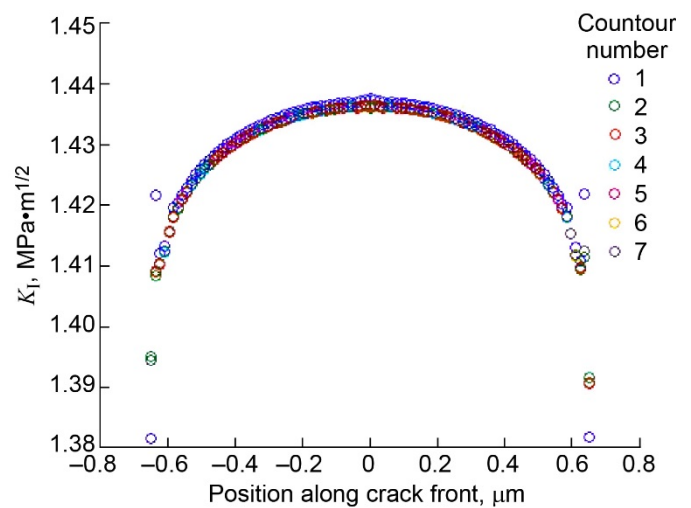


Figure 9.—Calculated mode I stress intensity factor  $K_I$  values across crack front for HfO<sub>2</sub>-Si microcantilever beams.

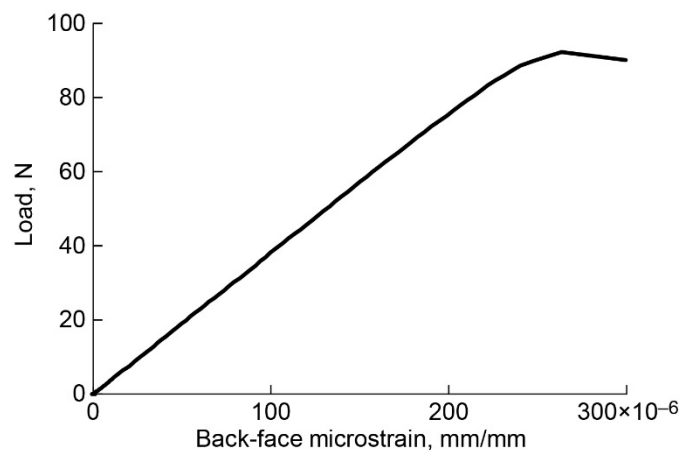


Figure 10.—Typical load versus back-face strain collected during HfO<sub>2</sub>-Si single-edge V-notched beam testing.



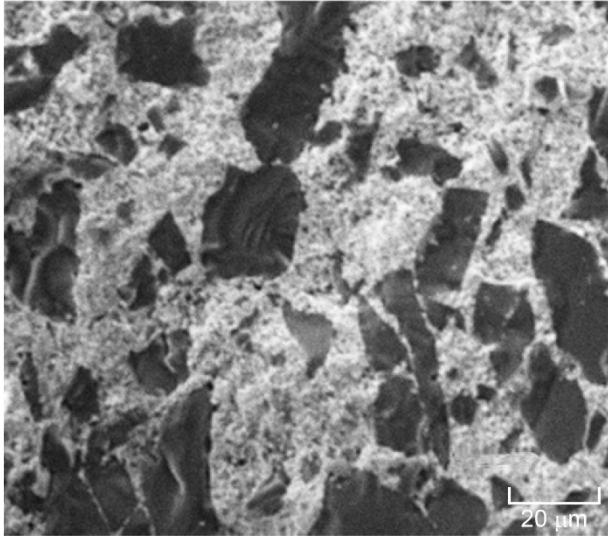


Figure 11.—Fracture surface of bulk HfO<sub>2</sub>-Si single-edge V-notched beam specimen. Light color is HfO<sub>2</sub>-rich phase, and dark color is Si-rich phase.

## 4.0 Discussion

This section analyzes the results of the microcantilever beam tests and discusses the fracture toughness of HfO<sub>2</sub>-Si; specifically, the effects of crack geometry and microstructure as well as size of the test specimen and limitations of the test method. Finally, results are compared with those from the bulk specimen SEVNB tests.

### 4.1 Crack Geometry Effect on Calculation of Fracture Toughness

Typical fracture toughness test specimens, such as single-edge notched beams or chevron notched beams, utilize well defined crack geometries for accurate determination of specimen fracture toughness. Because of insufficient milling, the starter notch of most test specimens had an irregular geometry. The authors' hypothesized that this would severely affect and/or invalidate the tests; however, the consistent results of this study and their agreement with literature suggest that the irregular geometry did not significantly affect the results or conclusions. This suggests two possibilities: (1) Pop-in events produced crack fronts of fairly regular geometry; that is, a straight front or (2) Pop-in events produced irregular crack fronts, but the calculation of  $K_I$  is relatively insensitive to this irregularity, possibly because of the irregularity's size in comparison to the overall crack length. The fracture surfaces of the HfO<sub>2</sub>-rich specimens supports the former, whereas those of the Si-rich specimens support the latter. The incomplete milling of the chevron in most samples does suggest that the tested specimens were influenced by milling damage. The most

important milling damage affecting the fracture toughness is mainly due to the implantation stresses that are compressive in nature and have been shown to reduce the effective stress at the crack tip, leading to a slight overestimation of  $K_{IC}$  (Ref. 10).

### 4.2 Microstructure Effect on Fracture Toughness

The different fracture mechanisms observed in the HfO<sub>2</sub>- and Si-rich phases appear to have contributed to significantly different behavior at the microscale. The small scatter and cleavage fracture of the Si-rich samples does not indicate the existence of any toughening effect at the scale of the microcantilevers. However, the HfO<sub>2</sub>-rich samples, when compared with each other, exhibit a range of toughness values that appear consistent with R-curve behavior when viewing  $K_C$  as a function of crack extension, where crack extension is defined as the distance between the apex of the chevron and the position of the crack front used in the FE models. Figure 12 shows this crack extension dependent toughening behavior as a pseudo-R-curve. However, plotting  $K_C$  as a function of the wake area results in this trend disappearing as shown in Figure 13. These plots vary from traditional R-curves in that their construction involves multiple samples with slightly different crack front and wake geometries rather than specimens with identical geometry. This difference could result in an R-curve of different shape as it has been found that measured R-curves are dependent on the wake region of an extending crack (Ref. 23). However, the experimental and numerical compliances match to within a few percent, and given that the FEM did not include wake-zone tractions, toughening from wake-zone tractions can be excluded as the cause of this behavior. For wake-zone tractions to be present, the model compliance for the same crack length would have to be significantly higher than experiment because the bridging stresses in the wake zone would reduce the compliance of the specimen. Knehans and Steinbrech found through renotching experiments that the removal of the wake zone of an extended crack would reduce the toughness back to its precrack extension value (Ref. 24). Further investigation conclusively proved the mechanism of R-curve behavior to be frictional contact of grains within the crack wake zone and that grain size has a significant effect on the magnitude of the toughening (Refs. 25 and 26). Hu and Wittmann found that this wake zone also contributed to changing the compliance of the specimen relative to a notched specimen of the same crack length (Ref. 27). Also, the lack of a rising  $K_C$  with increasing wake area also casts doubt on the presence of R-curve behavior. For toughening behavior to be present,  $K_C$  must rise with both crack extension and wake area.

These explanations indicate that Figure 12 represents only a coincidental trend between crack extension and  $K_C$  and would

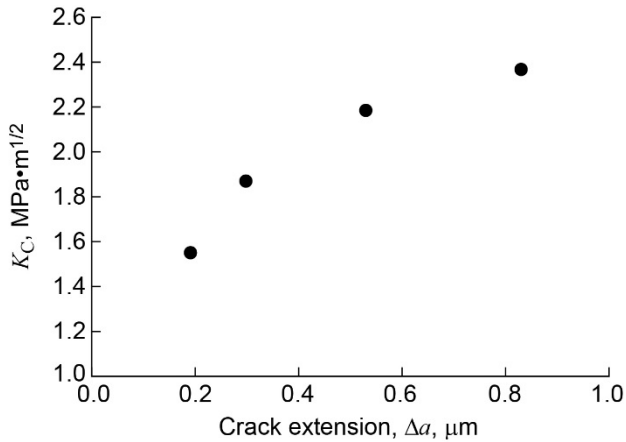


Figure 12.—Pseudo-R-curve plot compiled with multiple HfO<sub>2</sub>-rich HfO<sub>2</sub>-Si samples.

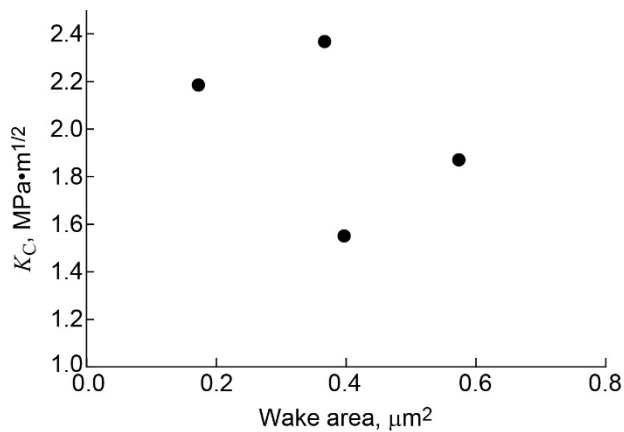


Figure 13.—Fracture toughness  $K_C$  plotted as function of wake-zone area for HfO<sub>2</sub>-rich HfO<sub>2</sub>-Si specimens.

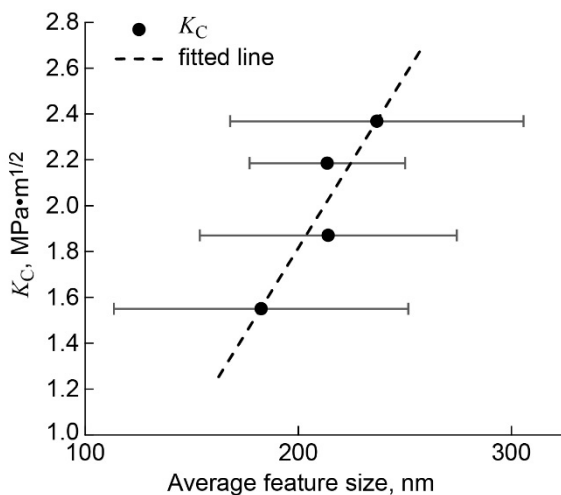


Figure 14.— $K_C$  plotted against average feature size along crack front. Error bars represent standard deviation for each HfO<sub>2</sub>-rich HfO<sub>2</sub>-Si sample.

disappear with a larger number of samples. However, a thorough investigation of R-curve behavior would require an additional study with identical specimen notch geometries to more accurately compare between samples, and ideally, compliance calibration of such specimens would enable the measurement of fracture toughness as a function of crack length for each specimen.

One likely explanation for the scatter in  $K_C$  is the heterogeneity in the HfO<sub>2</sub>-rich microstructure at the scale of the test specimens. Comparing calculated  $K_C$  with the average feature size along the crack front (Figure 14) reveals an apparent trend of increasing  $K_C$  with increasing feature size. Here, a feature is defined as being either a grain or cluster of grains that the crack deflected around. According to crack tip deflection models (Ref. 28), toughening is independent of particle size, provided the effect is averaged over the microstructure. Clearly, the scale of the specimens in relation to the grain size is too small to consider each tested specimen as having sampled a large enough area to be representative of the microstructure. The crack deflection angles appear to be larger in the case of the larger features and could account for the observed trend, but quantification is difficult with fracture surfaces compared with crack profiles. Mueller et al. tested nanocrystalline alumina with chevron-notched samples and observed little scatter, although their fracture surfaces appear more homogeneous in both shape and fracture features than the HfO<sub>2</sub>-rich samples in this study (Ref. 12). The source of this heterogeneity could be the distribution of HfO<sub>2</sub> and HfSiO<sub>4</sub> within each specimen, although as stated before, the low phase contrast of the fracture surfaces prevented determination of their explicit roles. Though it is true that R-curve behavior has been found to depend on grain size, it seems unlikely that such a broad range in toughening between the tested samples would be expected for the relatively small change in feature sizes observed here. It is likely that the scatter in  $K_C$  is due to a combination of fracture feature size and distribution of HfO<sub>2</sub> and HfSiO<sub>4</sub>.

### 4.3 Method Limitations

The measurement of fracture toughness at the microscale is inherently limited to capturing toughening mechanisms of the same or smaller scale than the test specimens (Ref. 29). This implies that the current method cannot capture effects that occur at dimensions larger than a couple of microns. These effects could include crack tip deflection at HfO<sub>2</sub>-Si phase boundaries and the possibility of intergranular fracture in the Si-rich phase, which could not be captured because of the larger grain sizes. Additionally, heterogeneity in the HfO<sub>2</sub>-rich microstructure appears to cause significant scatter in the results. Although the sample size of this study is small, an increased number of samples

would increase the confidence of a mean toughness, but not eliminate the core issue of the dimension of the test specimens relative to the microstructural heterogeneities. The dimension of the HfO<sub>2</sub>-rich phases, ~20 to 30 μm in diameter, in addition to their apparent heterogeneity, limits one's ability to conduct a single test that reliably reproduces an average toughness. Instead, a range of values are to be expected depending on the specimen.

#### 4.4 Comparisons With Bulk Specimens

SEVNB tests on a similarly prepared sample yielded an average  $K_{IC}$  of 1.1 MPa·m<sup>1/2</sup> (see Sec. 3.4). Comparison of the bulk tests and microscale tests offers two observations: First, the Si-rich-phase  $K_{IC}$  of 1.36 MPa·m<sup>1/2</sup> is ~24 percent larger than the bulk  $K_{IC}$ , lending some evidence towards compressive ion implantation stresses artificially increasing the microscale fracture toughness. Second, the HfO<sub>2</sub>-rich-phase  $K_{IC}$  of 1.99 MPa·m<sup>1/2</sup> is almost double that of the bulk  $K_{IC}$ , although the lower end of the 95% confidence interval, 1.42 MPa·m<sup>1/2</sup>, is much more in line with the bulk specimens. Given that the bulk specimen fracture surfaces had ~60 percent HfO<sub>2</sub>-rich fracture and ~40 percent Si-rich fracture, the bulk fracture should be representative of the contributions from both phases. This then suggests that the microscale results are overestimating the  $K_{IC}$

of both phases by 0.2 to 0.9 MPa·m<sup>1/2</sup>. Although the impact of implantation stresses is not evaluated here, it is possible they could be contributing to this elevation in  $K_{IC}$ . It is apparent, though, that a larger number of samples and more uniform notch geometry are needed to have greater confidence in the microcantilever results.

## 5.0 Conclusions

Microcantilever fracture specimens were used to evaluate the microscale fracture toughness of the HfO<sub>2</sub>-rich and Si-rich phases in an HfO<sub>2</sub>-Si environmental barrier coating. Numerical calculations were done to calculate  $K_I$  values for each test specimen to reasonable accuracy despite irregular crack geometry. Microstructural heterogeneity similar in dimension to the microcantilevers, perhaps due to the distribution of HfO<sub>2</sub> and HfSiO<sub>4</sub> and average fracture feature size, appeared to have caused significant scatter in the HfO<sub>2</sub>-rich-phase specimens. Comparison with bulk fracture tests suggests that the microscale tests overestimate  $K_{IC}$  of the Si- and HfO<sub>2</sub>-rich phases by ~0.2 to 0.9 MPa·m<sup>1/2</sup>. It is hypothesized that implantation stresses could play a role, but at minimum a larger number of samples and more-uniform notch geometry are needed for confidence in the microscale experiments.



## Appendix—Load-Displacement Fracture Demonstration

This appendix includes a sequence of video images from a load-displacement test; each image correlates with the load-displacement data shown. To illustrate this, a short explanation is given in Figure 15 for a Si-rich HfO<sub>2</sub>-Si specimen. Typically, elastic loading (Figure 15(a)) was

observed prior to a pop-in event in which a significant load drop and corresponding change in compliance occurred at constant displacement (Figure 15(b)). Continued loading is typically linear prior to unstable fracture (Figure 15(c)).

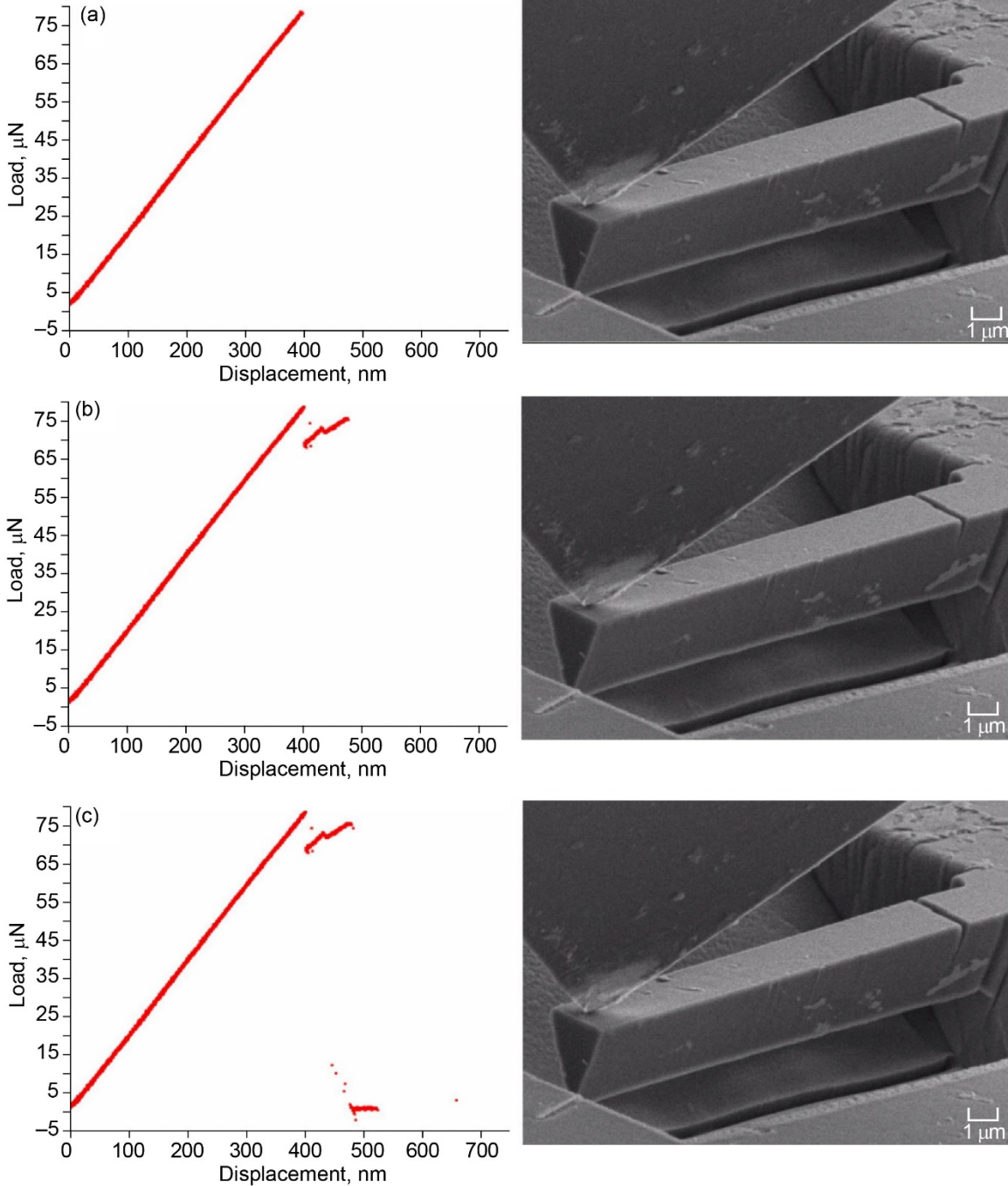


Figure 15.—Video image snapshots along with their respective load-displacement data for Si-rich HfO<sub>2</sub>-Si microcantilever test specimen. (a) Before pop-in. (b) After pop-in. (c) After fracture with significant crack extension.

## References

1. Lee, Kang N.; Fox, Dennis S.; and Bansal, Narottam P.: Rare Earth Silicate Environmental Barrier Coatings for SiC/SiC Composites and Si<sub>3</sub>N<sub>4</sub> Ceramics. *J. Eur. Ceram. Soc.*, vol. 25, 2005, pp. 1705–1715.
2. Spitsberg, Irene; and Steibel, Jim: Thermal and Environmental Barrier Coatings for SiC/SiC CMCs in Aircraft Engine Applications. *Int. J. Appl. Ceram. Technol.*, vol. 1, no. 4, 2004, pp. 291–301.
3. Zhu, Dongming: Advanced Environmental Barrier Coatings for SiC/SiC Ceramic Matrix Composite Turbine Components. *Engineered Ceramics: Current Status and Future Prospects*, Tatsuki Ohji and Mrityunjay Singh, eds., John Wiley & Sons, Inc., Hoboken, NJ, 2015, pp. 187–202.
4. Becher, Paul F.: Microstructural Design of Toughened Ceramics. *J. Am. Ceram. Soc.*, vol. 74, no. 2, 1991, pp. 255–269.
5. Sebastiani, M., et al.: A Novel Pillar Indentation Splitting Test for Measuring Fracture Toughness of Thin Ceramic Coatings. *Philos. Mag.*, vol. 95, no. 16–18, 2015, pp. 1928–1944.
6. Liu, S., et al.: Measuring the Fracture Resistance of Hard Coatings. *Appl. Phys. Lett.*, vol. 102, no. 17, 2013, p. 171907.
7. Best, James P., et al.: Small-Scale Fracture Toughness of Ceramic Thin Films: The Effects of Specimen Geometry, Ion Beam Notching and High Temperature on Chromium Nitride Toughness Evaluation. *Philos. Mag.*, vol. 96, no. 32–34, 2016, pp. 3552–3569.
8. Gong, Jicheng; and Wilkinson, Angus J.: Anisotropy in the Plastic Flow Properties of Single-Crystal  $\alpha$  Titanium Determined From Micro-Cantilever Beams. *Acta Mater.*, vol. 57, no. 19, 2009, pp. 5693–5705.
9. Tatami, Junichi, et al.: Local Fracture Toughness of Si<sub>3</sub>N<sub>4</sub> Ceramics Measured Using Single-Edge Notched Microcantilever Beam Specimens. *J. Am. Ceram. Soc.*, vol. 98, no. 3, 2015, pp. 965–971.
10. Norton, A.D., et al.: Microcantilever Investigation of Fracture Toughness and Subcritical Crack Growth on the Scale of the Microstructure in Al<sub>2</sub>O<sub>3</sub>. *J. Eur. Ceram. Soc.*, vol. 35, no. 16, 2015, pp. 4521–4533.
11. Volkert, C.A.; and Minor, A.M.: Focused Ion Beam Microscopy and Micromachining. *MRS Bull.*, vol. 32, no. 5, 2007, pp. 389–399.
12. Mueller, M.G., et al.: Fracture Toughness Testing of Nanocrystalline Alumina and Fused Quartz Using Chevron-Notched Microbeams. *Acta Mater.*, vol. 86, 2015, pp. 385–395.
13. Zagar, Goran, et al.: Fracture Toughness Measurement in Fused Quartz Using Triangular Chevron-Notched Micro-Cantilevers. *Scr. Mater.*, vol. 112, 2016, pp. 132–135.
14. Sola, F.; and Dynys, F.W.: Probing the Mechanical Properties and Microstructure of WSi<sub>2</sub>/Si<sub>x</sub>Ge<sub>1-x</sub> Multiphase Thermoelectric Material by Nanoindentation, Electron and Focused Ion Beam Microscopy Methods. *J. Alloys Compd.*, vol. 633, 2015, pp. 165–169.
15. Sola, F.; and Bhatt, R.: Mapping the Local Modulus of Sylramic Silicon Carbide Fibers by Nanoindentation. *Mater. Lett.*, vol. 159, 2015, pp. 395–398.
16. Watwood, V.B., Jr.: The Finite Element Method for Prediction of Crack Behavior. *Nucl. Eng. Des.*, vol. 11, no. 2, 1970, pp. 323–332.
17. Barsoum, Roshdy S.: On the Use of Isoparametric Finite Elements in Linear Fracture Mechanics. *Int. J. Numer. Methods Eng.*, vol. 10, no. 1, 1976, pp. 25–37.
18. Rice J.R.: A Path Independent Integral and the Approximate Analysis of Strain Concentration by Notches and Cracks. *J. Appl. Mech.*, vol. 35, 1968, pp. 379–386.
19. Shih, C.F.; and Asaro, R.J.: Elastic-Plastic Analysis of Cracks on Bimaterial Interfaces: Part I—Small Scale Yielding. *J. Appl. Mech.*, vol. 55, 1988, pp. 299–316.
20. International Organization for Standardization: Fine Ceramics (Advanced Ceramics, Advanced Technical Ceramics)—Test Methods for Fracture Toughness of Monolithic Ceramics—Single-Edge V-Notch Beam (SEVNB) Method—Second Edition. ISO 23146, 2012.
21. Hunter, O.; Scheidecker, R.W.; and Tojo, Setsuo: Characterization of Metastable Tetragonal Hafnia. *Ceramurg. Int.*, vol. 5, no. 4, 1979, pp. 137–142.
22. Ritchie, Robert O.: Failure of Silicon: Crack Formation and Propagation. Presented at the 13th Workshop on Crystalline Solar Cell Materials and Processes, Vail, CO, 2003.
23. Sakai, Mototsugo; and Bradt, Richard C.: The Crack Growth Resistance Curve of Non-Phase-Transforming Ceramics. *J. Ceram. Soc. Jpn.*, vol. 96, no. 1116, 1988, pp. 801–809.
24. Knehans, R.; and Steinbrech, R.: Memory Effect of Crack Resistance During Slow Crack Growth in Notched Al<sub>2</sub>O<sub>3</sub> Bend Specimens. *J. Mater. Sci. Lett.*, vol. 1, 1982, pp. 327–329.
25. Hubner, H.; and Jillek, W.: Sub-Critical Crack Extension and Crack Resistance in Polycrystalline Alumina. *J. Mater. Sci.*, vol. 12, 1977, pp. 117–125.
26. Hay, J.C.; and White, K.W.: Crack Face Bridging Mechanisms in Monolithic MgAl<sub>2</sub>O<sub>4</sub> Spinel Microstructures. *Acta Metall. Mater.*, vol. 40, no. 11, 1992, pp. 3017–3025.
27. Hu, X.Z.; and Wittmann, F.H.: Fracture Process Zone and Kr-Curve of Hardened Cement Paste and Mortar. *Fracture of Concrete and Rock: Recent Developments*, Elsevier Science Publishing Co., London, 1989.

28. Faber, K.T.; and Evans, A.G.: Crack Deflection Processes—I. Theory. *Acta Metall.*, vol. 31, no. 4, 1983, pp. 565–576.
29. Robertson, Andrew L.; and White, Ken W.: Microscale Fracture Mechanisms of a Cr<sub>3</sub>C<sub>2</sub>-NiCr HVOF Coating. *Mater. Sci. Eng. A*, vol. 688, 2017, pp. 62–69.







